SPECIALISED IMAGING

RESEARCH ARTICLE

Probing the nanoscale: the rst contact of an impacting drop

UK (Head Office / Factory)
6 Harvington Park,
Pitstone Green Business Park
Pitstone. LU7 9GX England
Tel **+44 (0) 1442 827728**

USA
Specialised Imaging Inc.
40935 County Center Dr. Suite D
Temecula, CA 92591, USA
Tel **+1 951-296-6406**

GERMANY
Hauptstr. 10,
82275 Emmering
Germany
Tel **+49 8141 666 89 50**

specialised-imaging.com **info@specialised-imaging.com**

FM 87429 ISO9001:2015

THE QUEEN'S AWARDS FOR ENTERPRISE: INNOVATION 2016

CrossMark

J. Fluid Mech. (2015), *vol.* 785, R2, doi:10.1017/jfm.2015.643

JFM RAPIDS
journals.cambridge.org/rapids

Probing the nanoscale: the first contact of an impacting drop

E. Q. Li[1], **I. U. Vakarelski**[1] **and S. T. Thoroddsen**[1,†]

[1]Division of Physical Sciences and Engineering and Clean Combustion Research Center, King Abdullah University of Science and Technology (KAUST), Thuwal 23955-6900, Saudi Arabia

(Received 12 September 2015; revised 25 October 2015; accepted 28 October 2015)

When a drop impacts onto a solid surface, the lubrication pressure in the air deforms its bottom into a dimple. This makes the initial contact with the substrate occur not at a point but along a ring, thereby entrapping a central disc of air. We use ultra-high-speed imaging, with 200 ns time resolution, to observe the structure of this first contact between the liquid and a smooth solid surface. For a water drop impacting onto regular glass we observe a ring of microbubbles, due to multiple initial contacts just before the formation of the fully wetted outer section. These contacts are spaced by a few microns and quickly grow in size until they meet, thereby leaving behind a ring of microbubbles marking the original air-disc diameter. On the other hand, no microbubbles are left behind when the drop impacts onto molecularly smooth mica sheets. We thereby conclude that the localized contacts are due to nanometric roughness of the glass surface, and the presence of the microbubbles can therefore distinguish between glass with 10 nm roughness and perfectly smooth glass. We contrast this entrapment topology with the initial contact of a drop impacting onto a film of extremely viscous immiscible liquid, where the initial contact appears to be continuous along the ring. Here, an azimuthal instability occurs during the rapid contraction at the triple line, also leaving behind microbubbles. For low impact velocities the nature of the initial contact changes to one initiated by ruptures of a thin lubricating air film.

Key words: contact lines, drops and bubbles, fingering instability

1. Introduction

The impact of a drop onto a solid is fundamental in many natural and industrial processes. One important aspect of the deposition is the entrapment of a bubble under the centre of the drop. It can have a detrimental effect on the uniformity in coating processes and affect conduction or conductivity through the interface between a solidified drop and the substrate. This central bubble was first observed in snapshot

† Email address for correspondence: sigurdur.thoroddsen@kaust.edu.sa

© Cambridge University Press 2015

photographs (Chandra & Avedisian 1991; Thoroddsen & Sakakibara 1998), but Thoroddsen *et al.* (2005) used high-speed video to image the initial entrapment of the air disc and modelled its subsequent contraction into the central bubble. They also identified a dark ring, which often marked the initial diameter of the air disc, proposing that it was due to the trapping of microbubbles.

The rapid contraction of the air disc can also leave a small drop at the centre of the bubble, when the converging capillary waves touch the dry substrate. This drop was imaged through the bottom glass by Thoroddsen *et al.* (2005) and later verified by Lee *et al.* (2012) using X-rays.

Driscoll & Nagel (2011) and Liu, Tan & Xu (2013) used interferometry with approximately 7 μs time resolution to observe the compression of the air disc for high impact velocities. Subsequently, Li & Thoroddsen (2015) used interferometry with 200 ns time resolution to capture the entire compression and rebounding of the air disc.

The theoretical treatment of the air-cushioning, started by Smith, Li & Wu (2003), is based on balancing the viscous lubrication in the thin air layer and the rapid deceleration of the drop inertia. Korobkin, Ellis & Smith (2008) added two deformable surfaces and Hicks & Purvis (2010) reformulated the above 2-D theories for the axisymmetric case, to allow quantitative comparison with theory. They predicted the initial radius of the air disc at first contact L_o, as (Hicks *et al.* 2012; Hicks & Purvis 2013)

$$L_o = 3.8 \left(\frac{4\mu_g}{\rho_\ell V} \right)^{1/3} R^{2/3}, \tag{1.1}$$

where μ_g is the gas viscosity, ρ_ℓ is the liquid density, V is the impact velocity of the drop and R is the drop radius. This formula is in perfect correspondence with the recent experiments of Li & Thoroddsen (2015), if one uses the bottom radius of curvature of the drop R_b for R. This is mandated by the significant shape oscillations of the large water drops used in those experiments.

Thoroddsen *et al.* (2005) measured the size of the central bubble for high impact velocities, but for low impact velocities, Bouwhuis *et al.* (2012) identified a local parameter, where the size of the entrapped bubble is maximum.

Mandre, Mani & Brenner (2009) investigated the compressibility of the air, which occurs for higher impact velocities. The amount of compression is determined by a compressibility factor

$$\epsilon^{-1} = \frac{(RV^7\rho_\ell^4/\mu_g)^{1/3}}{P_{atm}}, \tag{1.2}$$

where P_{atm} is the static atmospheric pressure. If $\epsilon^{-1} \gg 1$ one expects significant compression of the air disc. For adiabatic compression the 2-D theory of Mandre *et al.* (2009) predicts that the air-layer thickness at the centreline reduces as $H^*/(R\,St^{2/3}) \sim \epsilon^{1/3}$, where, following recent nomenclature, St is the inverse of the conventional Stokes number, i.e. $St = \mu_g/(\rho_\ell RV)$. The experiments in Li & Thoroddsen (2015) showed empirically that $H^*/(R_b St^{2/3}) = 4.2\epsilon^{0.40}$. They also showed that the radial motion U of the kink at the minimum gap (see the sketch in figure 1*a*) is in good agreement with the above theory, i.e. $U/V \sim St^{-1/3}$, see also Duchemin & Josserand (2011).

Mandre *et al.* (2009) and subsequent work by Mani, Mandre & Brenner (2010) and Mandre & Brenner (2012) suggested the intriguing possibility that an impacting drop could skate on a thin layer of air and splash without ever touching the solid surface.

However, the entrapment of the central air disc and its subsequent contraction into a bubble (Thoroddsen *et al.* 2005), mandate a contact with the solid surface. Even though the skating on a thin layer of air may have little bearing on splashing, it is important for rebounding of the drop for small impact velocities, which is observed even for hydrophilic surfaces (Kolinski, Mahadevan & Rubinstein 2014; de Ruiter *et al.* 2015). de Ruiter *et al.* (2015) used smooth glass surfaces to find the maximum impact velocity where rebound without contact can take place, characterized by Weber numbers $We = \rho_\ell R V^2/\sigma$ below 4, where σ is the surface tension. Mandre & Brenner (2012) highlighted the importance of surface roughness, formulating conditions when the minimum air gap will reach nanometric thickness and minuscule asperities could rupture the film.

Herein, we apply ultra-high-speed direct imaging to investigate the nature of the initial contact of the drop liquid with the solid surface. In particular, we identify the mechanism behind the formation of the characteristic ring of microbubbles which conveniently marks the location of the initial contact. Thereby, our imaging reveals a new level of complexity in this fundamental process, which can only be revealed by the fastest imaging ever performed of this process.

2. Experimental set-up

2.1. *Optical and imaging set-up*

The experimental configuration is sketched in figure 1(*b*) and is essentially the same as in Li & Thoroddsen (2015), with imaging through the bottom glass plate. We use transmitted light or reflective interferometry to measure the thickness of the air layer $h(r)$, while allowing imaging of the contact region. The pulsed monochromatic illumination ($\lambda_{light} = 640$ nm) is produced by 180 laser diodes (SI-LUX640), one per video frame. This gives a depth resolution of $\lambda_{light}/4 = 160$ nm between adjacent dark and bright fringes. We use long-distance microscopes, primarily a Leica (Z16 APO), with pixel resolution down to 1.04 μm px^{-1}. The rapid surface motions during first contact require ultra-high-speed video, acquired with the Kirana-05M from Specialized Imaging in Tring, UK (Crooks *et al.* 2013), at frame rates up to 5 million f.p.s. The extreme 200 ns time resolution allows us to follow individual fringes between video frames and eliminates some of the ambiguity at lower frame rates, which has required colour interferometry to get absolute layer thicknesses (de Ruiter *et al.* 2012; van der Veen *et al.* 2012). Thickness profiles with multiple local minima, as well as rebounding non-contact cases, will still need the two-colour technique to get absolute thicknesses (de Ruiter *et al.* 2012).

A few experiments were performed with even larger optical magnification by using a 50× Mitutoyo objective, for a pixel resolution of 0.566 μm. The resulting images were not as clear due to diffraction as well as the very narrow depth of focus (see figure 5).

The water drops used herein have an equivalent diameter of $D \simeq 5.2$ mm, which is significantly larger than the capillary length $a = \sqrt{\sigma/(\Delta\rho\, g)} \simeq 2.7$ mm, and therefore show large shape oscillations, which must be determined at impact. This is accomplished with side views using a Phantom V1610 CMOS video camera. Typical drop shapes are shown in figure 1(*c*). The impact velocities presented herein are between $V = 1.2$ and 4.2 m s^{-1}, corresponding to a range of Weber numbers $We = \rho R V^2/\sigma = 59$–$755$.

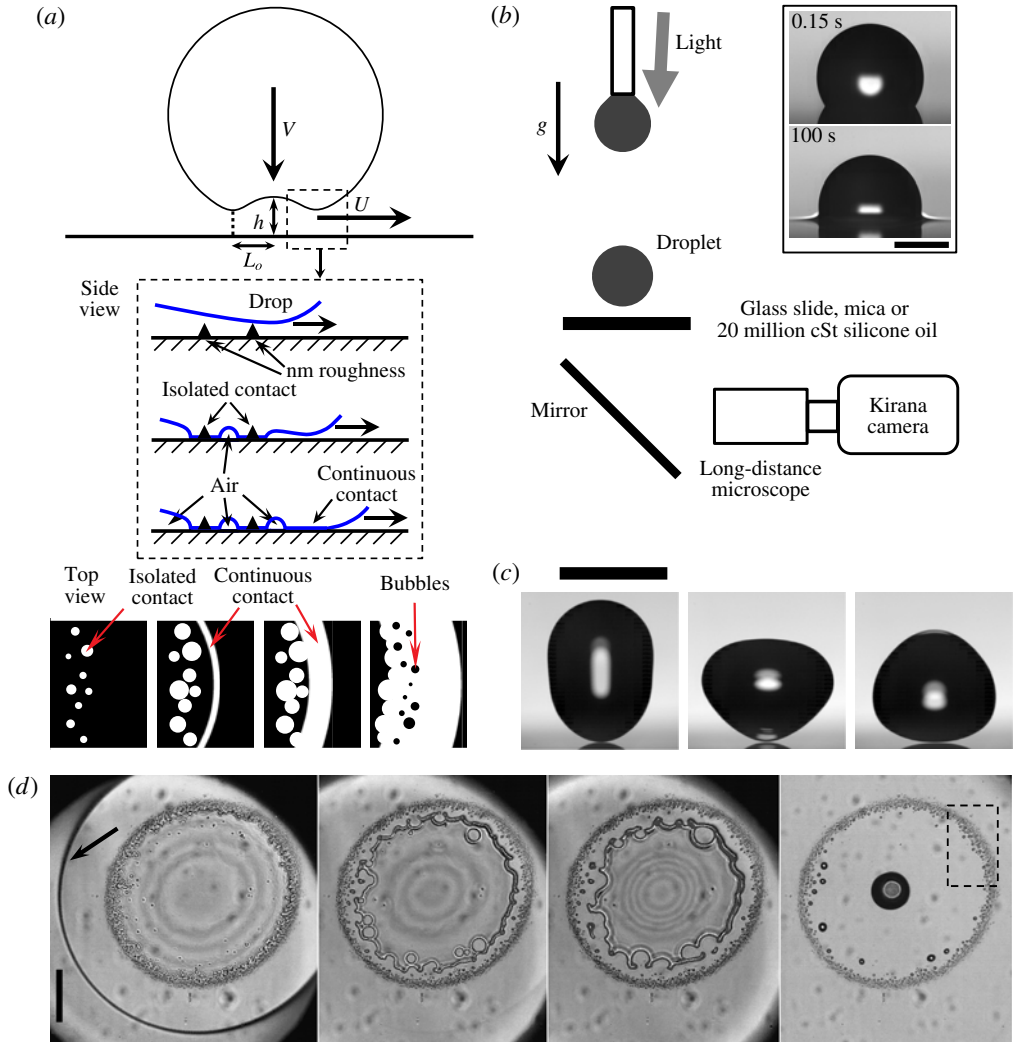

FIGURE 1. (*a*) Definition sketch, identifying the air-layer thickness $h(r)$ and the radial velocity U of the kink at the outer edge of the dimple, including, at the bottom, two schematics of the isolated contacts occurring before the fully wetted region, leading to the entrapment of microbubbles, from the side view and top view. (*b*) Sketch of the experimental set-up, showing the imaging through the substrate and the arrangement of the laser diodes with respect to the drop and video camera. The inset displays the shape of a small water drop gently deposited on top of a 20 million cSt silicone oil surface, to measure the contact angle, shown 0.15 and 100 s after contact. The scale bar is 500 μm. (*c*) Example shapes of the large water drop at impact. The scale bar is 5 mm. (*d*) Typical microbubbles marking the initial contact of a water drop impacting onto a dirty (as delivered uncleaned) glass microscope slide. Frames are shown at 2, 7, 12 and 400 μs from first contact, for $R_b = 7.3$ mm and $V = 4.59$ m s^{-1}, giving $We = 755$, $St = 5.8 \times 10^{-7}$ and $\epsilon^{-1} = 22$. The scale bar is 200 μm. The arrow in the first panel identifies the outer contact line. The dotted rectangle in the last panel identifies the approximate location of the viewing area in figure 3(*a*), for a different impact onto cleaned glass.

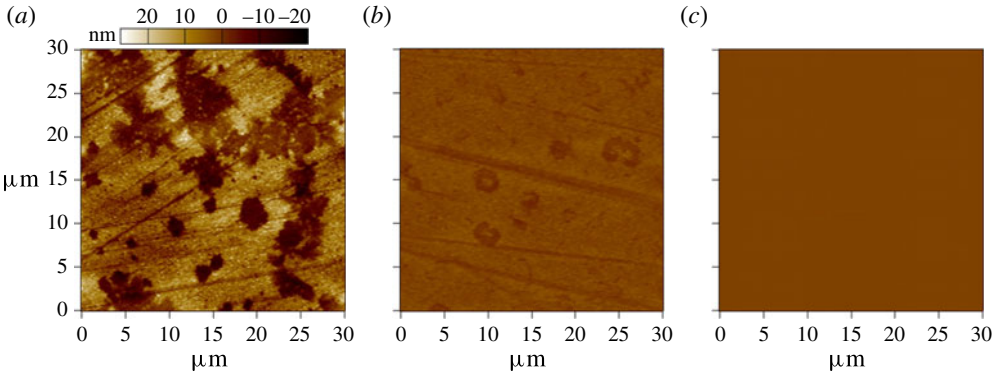

FIGURE 2. The roughness of the glass and mica surfaces: AFM topographic images of 30 × 30 μm regions of (*a*) Corning glass, (*b*) Fisher glass and (*c*) freshly cleaved mica surface. For the Corning glass, RMS = 7.3 nm, max. to min. = 49 nm; for the Fisher glass, RMS = 1.2 nm, max. to min. = 10 nm; for the mica, RMS < 0.5 nm. The supplementary material shows scans over larger surface areas (see the supplementary movies available at http://dx.doi.org/10.1017/jfm.2015.643).

2.2. *Glass and mica substrates*

We tested two different microscope-slide glass substrates, supplied by Corning (2947-75 × 50) and Fisher Scientific. The glass slides were cleaned in a sequence of ultrasonic baths of acetone, isopropanol and deionized water for 10 min each. Following this treatment, the contact angle of water on the glass was approximately 20°. Figure 1(*d*) shows an impact onto a dirty glass slide, i.e. one which has not been cleaned, showing much stronger air entrapment than for cleaned glass in what follows.

We also tested thin mica sheets which were attached to a glass slide with epoxy glue. The sheets were cleaved after every few drop impacts, to produce a fresh surface. This was done by depositing a Scotch tape onto the surface and rapidly peeling it off. A clear sign of successful peeling was that the tape would become smooth to the touch and lose its stickiness. Between drop impacts the surface was dried by blowing dry nitrogen, thereby removing any droplets or wet spots. Water fully wets the freshly cleaved mica.

Figure 2 shows atomic force microscope (AFM) measurements of the surface roughnesses of the three different surfaces. The two glass slides have differing roughnesses, with the mica surface perfectly smooth within the measurement accuracy.

2.3. *Ultra-viscous liquid substrate*

In addition to water drop impacts onto the glass substrates, described above, we also imaged impacts onto an extremely viscous liquid surface, immiscible to the water drop. Here, the idea is to use a liquid to eliminate any surface roughness or asperities. For this purpose we use a silicone oil of 20 million cSt (Clearco Products). The properties are given in table 1. This liquid is so viscous that it takes hours to flatten, under gravity, after it is scooped onto a solid surface. We therefore deposit a fixed weight (2 g) of the material onto a glass plate, which we then heat to 80 °C in an oven to make it spread overnight into a 1 mm thick circular patch. The contact angle of a small water drop gently deposited on the immiscible silicone oil was measured,

Fluid	Density ρ (kg m^{-3})	Viscosity μ (cP)	Surface tension σ (dyn cm^{-1})
Air (A)	1.2	0.0186	—
Water (W)	998	0.981	72.38
Silicone oil 20 000 000 cSt	970	19 400 000	21.2

TABLE 1. Properties of the fluids used in the experiments. The properties for the silicone oil are taken from the supplier's data sheets.

150 ms after contact, to be $\simeq 118°$, see the inset in figure 1(*b*). Contact angles are not well defined here as the triple line locally deforms the viscous surface (see Style *et al.* 2013).

3. Results

3.1. *Effect of glass roughness versus smooth mica*

Figure 3(*a*) shows a close-up view of the outer edge of the air disc, as it makes contact with the rougher glass (Corning). For orientation, see the approximate rectangle in figure 1(*d*), marked on a different impact. The second panel reveals isolated circular contacts, which occur slightly behind the continuous contact region which forms when the air-film thickness goes below some critical value. This region becomes visible in the third panel, see the sketch in figure 1(*a*). The localized contacts grow in size and merge, leaving microbubbles between them and the fully wetted outer region, the outer edge of which is marked with black arrows. Immediately following this, a rugged inner contact line forms and starts to contract into the central bubble. The fine dark spots left behind are the microbubbles, with a typical size of 2–5 μm. Figure 3(*b*) contrasts this with the impact onto a molecularly smooth mica sheet. Here, the initial contact appears uniformly around the periphery, with no obvious isolated circular contacts before continuous wetting. The contraction of the thin edge produces fine undulations in the azimuthal direction, but no isolated microbubbles are left behind during the retraction of the inner contact line. A similar influence of roughness is observed for other impact conditions, for impact velocities larger than the skating regime, i.e. for $St < 6 \times 10^{-6}$ or $We > 70$. The AFM measurements in figure 2 show that the Fisher glass is much smoother than the Corning glass, as is clearly evident in figure 3(*c*), where the contact is similar to that with the mica, and less than a handful of clearly identifiable local contacts are observed, leaving only one distinct microbubble. However, a fine ring of tiny microbubbles (white arrows) can be discerned from a careful inspection of the video, shown in the supplementary material, where we include two enhanced frames. In this case, the localized contacts and formation of the fully wetted region must occur within the 200 ns interframe time.

Consistent with this picture, figure 1(*d*) showed a much larger number of entrapped microbubbles for impact on a rougher uncleaned glass surface.

3.2. *Impact on ultra-viscous liquid substrate*

In a further attempt to reduce the surface roughness, we also tried impacts onto an ultra-viscous liquid film. Using a liquid surface one can minimize any asperities, other than possible dust settling on the surface. In figure 4(*d*) we first compare the thickness

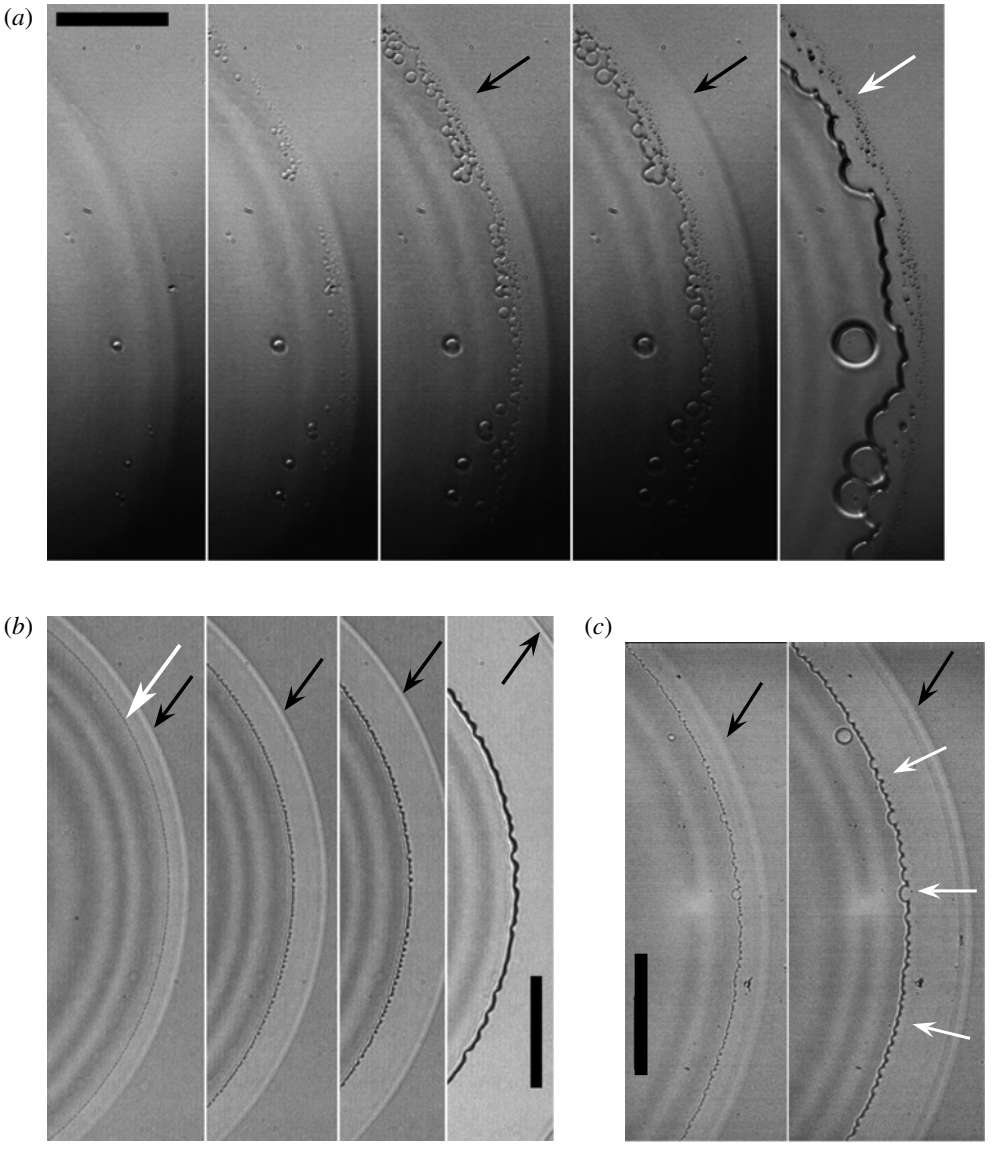

FIGURE 3. Comparison of the first contact of drops impacting on glass and mica surfaces. (*a*) Examples of the ring of microbubbles at the outer edge of the central contact on Corning glass, for a water drop with $D = 5.2$ mm, $R_b = 8.2$ mm and impact velocity $V = 2.43$ m s^{-1}, giving $St = 9.2 \times 10^{-7}$ ($\epsilon^{-1} = 5.98$, $We = 212$). Frames are shown at $t = -0.2$, 0, 0.2, 0.4 and 1.8 μs around first contact. The white arrow points out the ring of microbubbles left behind. (*b*) Impact on a molecularly smooth freshly cleaved mica surface, for $R_b = 4.1$ mm and impact velocity $V = 2.10$ m s^{-1} ($St = 2.1 \times 10^{-6}$, $\epsilon^{-1} = 3.37$, $We = 158$), shown at $t = 0$, 0.2, 0.4 and 1.6 μs from first contact. The white arrow points to the inner contact line. No microbubbles are left behind. (*c*) Impact on a cleaned Fisher microscope slide, shown at $t = 0$ and 0.4 μs for $R_b = 5.1$ mm, $V = 2.33$ m s^{-1} ($St = 1.5 \times 10^{-6}$, $\epsilon^{-1} = 4.6$, $We = 195$). The scale bars are all 100 μm. The white arrows, in the last panel, point out a faint ring of tiny bubbles, which can be better observed in an enhanced supplementary image and movie. The black arrows in all panels indicate the outer edge of the fully wetted contact.

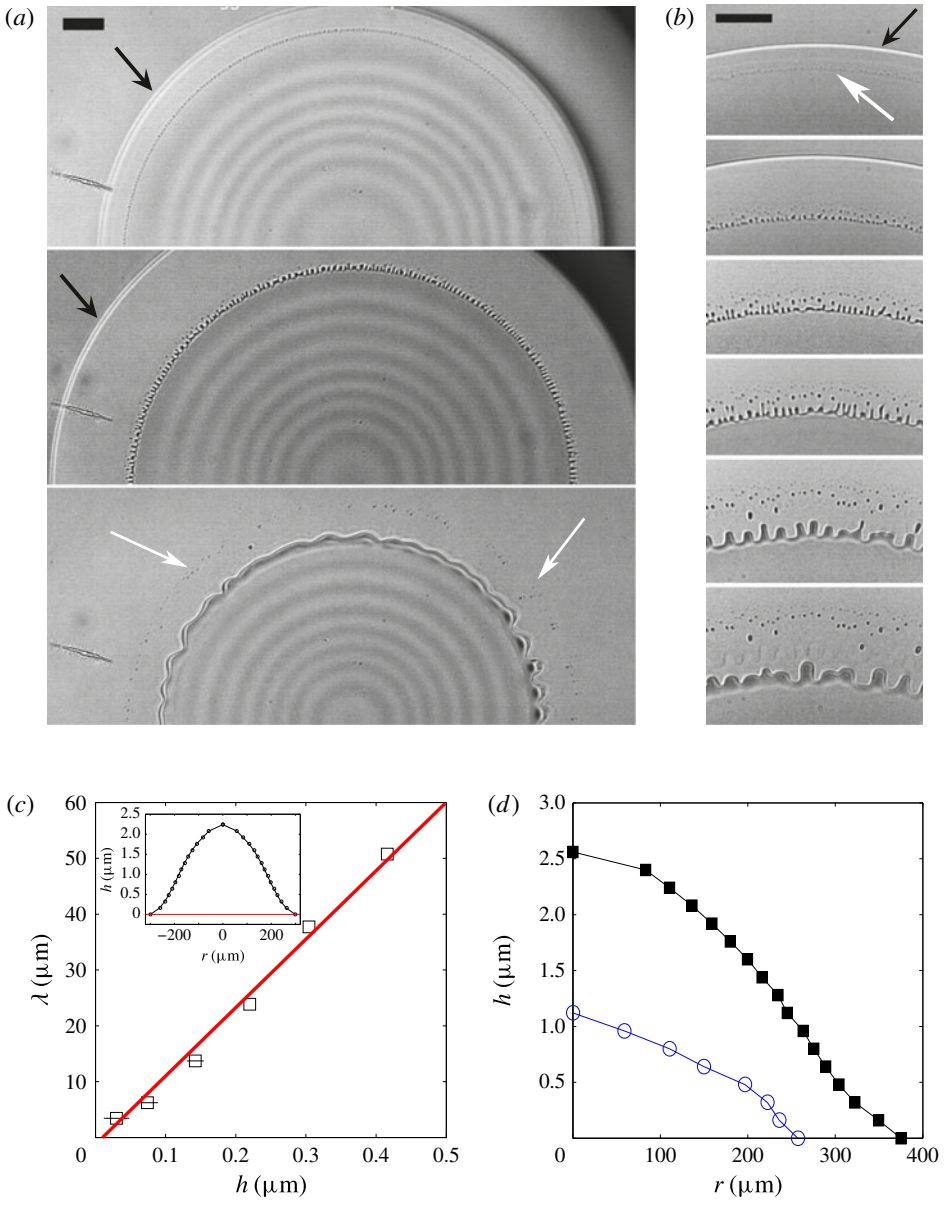

FIGURE 4. (*a*) The air disc under a water drop impacting onto a 20×10^6 cSt silicone oil surface, at velocity $V = 3.15$ m s^{-1} and $R_b = 2.4$ mm. Frames are shown at $t = 0.4$, 1.8 and 12.2 μs after first contact ($St = 2.4 \times 10^{-6}$, $\epsilon^{-1} = 7.5$, $We = 356$). The white arrows point out entrapped microbubbles. The black arrows in all panels identify the outer contact line. (*b*) Undulations and pinch-off of microbubbles at the contracting edge of the air disc, shown at $t = 0$, 1, 2, 3, 7.5 and 12.5 μs. The scale bars are 50 μm. The white arrow in the first panel identifies the inner contact line. (*c*) The azimuthal wavelength of the characteristic undulations at the edge of the contracting triple line versus the initial local thickness of the air film, shown in the inset. (*d*) Comparison of the air-film thickness profile for identical water drops ($V = 3.10$ m s^{-1}, $R_b = 4.0$ mm, $St = 1.5 \times 10^{-6}$, $\epsilon^{-1} = 8.3$, $We = 344$) impacting onto a Corning glass surface (open circles) and 20×10^6 cSt silicone oil (filled squares).

profiles $h(r)$ of the air layers for impacts of identical water drops onto Corning glass versus the ultra-viscous 20×10^6 cSt silicone oil. One striking difference between these two substrates is the greatly reduced compression of the gas, in the air disc, for impacts onto the viscous surface. The air disc on the ultra-viscous substrate is twice as thick and 1.5 times larger in diameter. Clearly, the compliance of the ultra-viscous substrate reduces the maximum pressure, and this is a testament to the large compression that occurs (Liu *et al.* 2013; Li & Thoroddsen 2015). This is further demonstrated during the subsequent rapid expansion of the air layer, which is observed for the impact onto the solid Corning glass surface, but is almost eliminated by the viscous substrate. Here, the more compressed air on the glass expands at the centreline by a factor of 2.3 from 1.12 to 2.56 μm, while on the silicone oil it expands by only a factor of 1.25 from 2.56 to 3.2 μm. Here, the added inertia of the substrate plays no role, like for the case of identical liquids (Bouwhuis *et al.* 2015).

Microbubbles are also left behind for this water-on-silicone-oil configuration. However, they arise not from localized contacts like in figure 3(*a*), but rather from an azimuthal instability of the rapidly moving triple line, as shown in figure 4(*b*). The wavelength λ of this instability follows the local thickness $h(r)$ of the air film (figure 4*c*) quite well, with $\lambda \simeq 120\, h(r)$. Here, $h(r)$ is determined from the interference fringes at first contact, as shown in the inset. The wavelength grows by merging of adjacent crests, while their tips shed microbubbles which become progressively larger. Similar bubble shedding is observed for thin air layers in Mesler entrainment, see figure 4 in Thoroddsen *et al.* (2012).

The contraction of the inner edge of the air disc starts at $u_{edge} = 10.1$ m s^{-1}, corresponding to a capillary number based on the water properties of $Ca = \mu\, u_{edge}/\sigma = 0.14$. The edge velocity slows as the edge thickens and the pinch-off of bubbles stops, after 13 μs, when $u_{edge} \simeq 3.45$ m s^{-1}, corresponding to $Ca = 0.048$. Regular undulations have here essentially disappeared when the edge has contracted to the radius where the original thickness was $h(r) \simeq 0.5$ μm.

The nature of this long-wavelength instability is unclear. The very long wavelength, compared with the layer thickness, appears to rule out a capillary Rayleigh instability of a thicker edge. Furthermore, λ is orders of magnitude smaller than the radius of the air disc, so we conclude that the azimuthal curvature of the triple line is not important. It should be kept in mind that the presence of the triple line, between the water and the high-viscosity liquid, has a strong effect on its contraction, greatly slowing it down (Li *et al.* 2014).

3.3. *Low impact velocity, skating and film ruptures*

For very low impact velocities, it has been shown that drops can skate on a thin layer of air (Kolinski *et al.* 2012) and even rebound without touching the substrate (Kolinski *et al.* 2014; de Ruiter *et al.* 2015). Such skating of the outer edge on a thin layer of air is indeed observed herein for low impact velocities. In the water-on-20-million-cSt configuration, this occurs when $St > \sim 5 \times 10^{-6}$, corresponding to $We < 70$. It should be kept in mind that this is for much larger We than the rebounding regime studied in de Ruiter *et al.* (2015). In our impact-velocity range, these films rupture and we do not look at rebounding. Figure 5 and a supplementary movie show such a low-impact-velocity case for a water drop on a 20×10^6 cSt silicone film. This thin gliding air layer then ruptures simultaneously at multiple locations around the periphery, merging into a band of ruptures, as marked by the arrows in figure 5(*a*). The original location of the ruptures is ∼50 μm behind the outer edge of the thin air layer. The edge

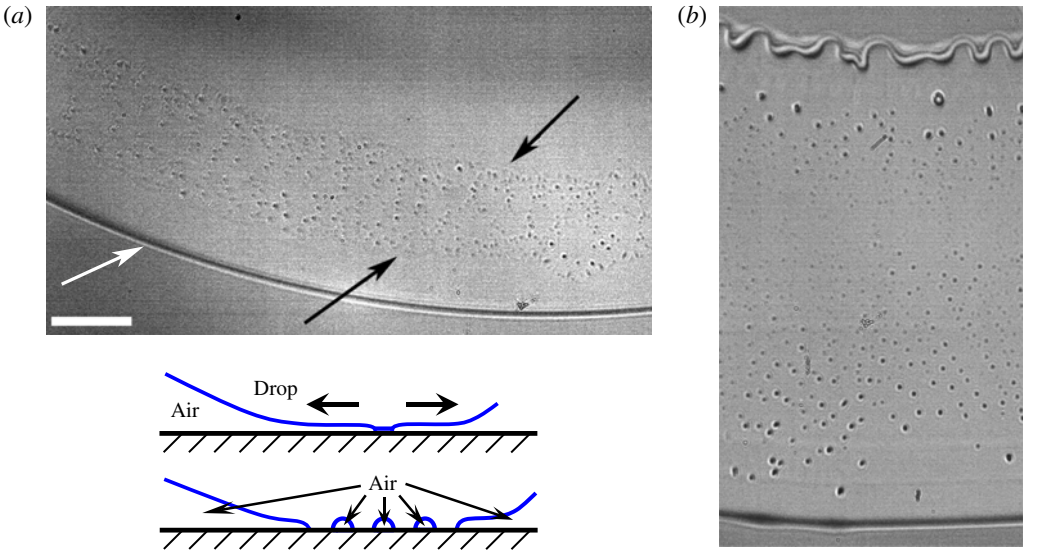

FIGURE 5. (*a*) Example of the rupture of the thin air film, under the gliding edge, for water on 20×10^6 cSt silicone oil, for low impact velocity $U = 1.28$ m s^{-1}, $R_b = 4.5$ mm ($St = 3.2 \times 10^{-6}$, $\epsilon^{-1} = 1.10$, $We = 59$). The two dark arrows point out the edges of the rupture zone, which is at a significant distance behind the outer moving edge of the gliding marked by a white arrow. The scale bar is 50 μm. Below is a sketch of the film rupture mechanism. (*b*) The band of microbubbles 11 μs after the start of ruptures in (*a*), when the entrapment of microbubbles has stopped and the rupture front has caught up with the outer edge of the thin air layer.

speed of the growing wet spots is measured at $\simeq$15 m s^{-1}, which is faster than the contracting edge in figure 4, which indicates a layer thickness much thinner than 100 nm. Numerous microbubbles are entrapped where these ruptures meet, thereby forming a band of contacts, which widens rapidly in the radial direction. The outer edge of this rupture zone moves faster than the edge of the air layer marking the spreading drop (white arrow in figure 5) and catches up with it after 9 μs in this realization. This eliminates the skating of the edge and the accompanying microbubble entrapment, leaving behind a 200 μm wide band of bubbles. The total number of visible microbubbles in this entire band around the full periphery is here estimated to be ~12 800, ranging in size from 1 to 5 μm. The bubble sizes are smallest near the first rupture, where the air layer should be thinnest (Beilharz *et al.* 2015), and grow larger towards the edges of the band (figure 5*b*). Such bands of bubbles have been observed for impacts of viscous drops in Thoroddsen *et al.* (2005), Thoroddsen, Takehara & Etoh (2010) and Palacios *et al.* (2012).

4. Discussion and conclusions

Herein, we have used ultra-fast video imaging to observe the first contact of an impacting drop with a solid or an extremely viscous substrate. Our results show that ~10 nm surface roughness promotes localized contacts slightly before full wetting is established, thereby leaving behind the previously observed ring of microbubbles (Thoroddsen *et al.* 2005). Impacts onto smoother glass reduce the sizes of these bubbles, and none are visible for impacts onto the molecularly smooth mica substrate,

at our optical resolution. However, the first contact on the mica shows fine azimuthal undulations, the origins of which remain a mystery, but we suggest that they are due to contact line dynamics.

Impacts onto the ultra-viscous silicone surface also leave a ring of microbubbles, not due to roughness, but through an azimuthal instability at the triple line, by tip streaming.

The theory of Mandre & Brenner (2012) (their figure 8*a*) presents the roughness needed to interfere with the lubricating air film for different impact conditions. For our water drop sizes and impact velocities, the very small roughness of the freshly cleaved mica sheets should be insufficient to break the lubricating films in figure 3(*b*). This implies that some phenomenon that is left out of their skating model is at play. We suggest that the ruptures are due to van der Waals forces, when the air film becomes significantly thinner than 100 nm, which we cannot measure with our optical set-up. The fact that ruptures arise simultaneously along the periphery and at the same radial distance, in figure 5(*a*), rules out isolated larger asperities as the trigger.

Furthermore, even for molecularly smooth mica surfaces the continuous contact shows that the skating solutions are not realized above a moderate impact velocity.

Acknowledgement

The work reported herein was funded by King Abdullah University of Science and Technology (KAUST). The AFM imaging was performed in the KAUST Microfluidics Thrust Area Labs.

Supplementary movies

Supplementary movies are available at http://dx.doi.org/10.1017/jfm.2015.643.

References

BEILHARZ, D., GUYON, A., LI, E. Q., THORAVAL, M.-J. & THORODDSEN, S. T. 2015 Antibubbles and fine cylindrical sheets of air. *J. Fluid Mech.* **779**, 87–115.

BOUWHUIS, W., HENDRIX, M. H. W., VAN DER MEER, D. & SNOEIJER, J. H. 2015 Initial surface deformations during impact on a liquid pool. *J. Fluid Mech.* **771**, 503–519.

BOUWHUIS, W., VAN DER VEEN, R. C. A., TRAN, T., KEIJ, D. L., WINKELS, K. G., PETERS, I. R., VAN DER MEER, D., SUN, C., SNOEIJER, J. H. & LOHSE, D. 2012 Maximal air bubble entrainment at liquid-drop impact. *Phys. Rev. Lett.* **109**, 264501.

CHANDRA, S. & AVEDISIAN, C. T. 1991 On the collision of a droplet with a solid surface. *Proc. R. Soc. Lond.* A **432**, 13–41.

CROOKS, J., MARSH, B., TURCHETTA, R., TAYLOR, K., CHAN, W., LAHAV, A. & FENIGSTEIN, A. 2013 Kirana: a solid-state megapixel uCMOS image sensor for ultrahigh speed imaging. *Proc. SPIE* **8659**, 865903.

DRISCOLL, M. M. & NAGEL, S. R. 2011 Ultrafast interference imaging of air in splashing dynamics. *Phys. Rev. Lett.* **107**, 154502.

DUCHEMIN, L. & JOSSERAND, C. 2011 Curvature singularity and film-skating during drop impact. *Phys. Fluids* **23**, 091701.

HICKS, P. D., ERMANYUK, E. V., GAVRILOV, N. V. & PURVIS, R. 2012 Air trapping at impact of a rigid sphere onto a liquid. *J. Fluid Mech.* **695**, 310–320.

HICKS, P. D. & PURVIS, R. 2010 Air cushioning and bubble entrapment in three-dimensional droplet impacts. *J. Fluid Mech.* **649**, 135–163.

HICKS, P. D. & PURVIS, R. 2013 Liquid–solid impacts with compressible gas cushioning. *J. Fluid Mech.* **735**, 120–149.

KOLINSKI, J. M., MAHADEVAN, L. & RUBINSTEIN, S. M. 2014 Drops can bounce from perfectly hydrophilic surfaces. *Eur. Phys. Lett.* **108**, 24001.

KOLINSKI, J. M., RUBINSTEIN, S. M., MANDRE, S., BRENNER, M. P., WEITZ, D. A. & MAHADEVAN, L. 2012 Skating on a film of air: drops impacting on a surface. *Phys. Rev. Lett.* **108**, 074503.

KOROBKIN, A. A., ELLIS, A. S. & SMITH, F. T. 2008 Trapping of air in impact between a body and shallow water. *J. Fluid Mech.* **611**, 365–394.

LEE, J. S., WEON, B. M., JE, J. H. & FEZZAA, K. 2012 How does an air film evolve into a bubble during drop impact? *Phys. Rev. Lett.* **109**, 204501.

LI, E. Q., AL-OTAIBI, S., VAKARELSKI, I,. U. & THORODDSEN, S. T. 2014 Satellite formation during bubble transition through an interface between immiscible liquids. *J. Fluid Mech.* **744**, R1.

LI, E. Q. & THORODDSEN, S. T. 2015 Time-resolved imaging of a compressible air disc under a drop impacting on a solid surface. *J. Fluid Mech.* **780**, 636–648.

LIU, Y., TAN, P. & XU, L. 2013 Compressible air entrapment in high-speed drop impacts on solid surfaces. *J. Fluid Mech.* **716**, R9.

MANDRE, S. & BRENNER, M. P. 2012. The mechanism of a splash on a dry solid surface. *J. Fluid. Mech.* **690**, 148–172.

MANDRE, S., MANI, M. & BRENNER, M. P. 2009 Precursors to splashing of liquid droplets on a solid surface. *Phys. Rev. Lett.* **102**, 134502.

MANI, M., MANDRE, S. & BRENNER, M. P. 2010 Events before droplet splashing on a solid surface. *J. Fluid. Mech.* **647**, 163–185.

PALACIOS, J., HERNÁNDEZ, J., GÓMEZ, P., ZANZI, C. & LÓPEZ, J. 2012 On the impact of viscous drops onto dry smooth surfaces. *Exp. Fluids* **52**, 1449–1463.

DE RUITER, J., LAGRAAUW, R., VAN DEN ENDE, D & MUGELE, F. 2015 Wettability-independent bouncing on flat surfaces mediated by thin air films. *Nat. Phys.* **11**, 48–53.

DE RUITER, J., OH, J. M., VAN DEN ENDE, D. & MUGELE, F. 2012 Dynamics of collapse of air films in drop impact. *Phys. Rev. Lett.* **108**, 074505.

SMITH, F. T., LI, L. & WU, G. X. 2003 Air cushioning with a lubrication/inviscid balance. *J. Fluid Mech.* **482**, 291–318.

STYLE, R. W., HYLAND, C., BOLTYANSKIY, R., WETTLAUFER, J. S. & DUFRESNE, E. R. 2013 Surface tension and contact with soft elastic solids. *Nat. Commun.* **4**, 2728.

THORODDSEN, S. T., ETOH, T. G., TAKEHARA, K., OOTSUKA, N. & HATSUKI, Y. 2005 The air-bubble entrapped under a drop impacting on a solid surface. *J. Fluid Mech.* **545**, 203–212.

THORODDSEN, S. T. & SAKAKIBARA, J. 1998 Evolution of the fingering pattern of an impacting drop. *Phys. Fluids* **10**, 1359–1374.

THORODDSEN, S. T., TAKEHARA, K. & ETOH, T. G. 2010 Bubble entrapment through topological change. *Phys. Fluids* **22**, 051701.

THORODDSEN, S. T., THORAVAL, M.-J., TAKEHARA, K. & ETOH, T. G. 2012 Micro-bubble morphologies following drop impacts onto a pool surface. *J. Fluid Mech.* **708**, 469–479.

VAN DER VEEN, R. C. A., TRAN, T., LOHSE, D. & SUN, C. 2012 Direct measurements of air layer profiles under impacting droplets using high-speed color interferometry. *Phys. Rev.* E **85**, 026315.